Journal of Rock Mechanics and Geotechnical Engineering 18 (2026) 3589–3605

Contents lists available at ScienceDirect

Journal of Rock Mechanics and Geotechnical Engineering

journal homepage: www.jrmge.cn

Full Length Article

Loading-unloading responses of non-persistent flawed granite subjected to cyclic disturbances

Tingting Liu [a,b], Chao Zhang [a], Luyang Ding [a,b,*], Kun Xu [a], Xinping Li [a,b], Wenxu Huang [a,b]

[a] School of Civil Engineering and Architecture, Wuhan University of Technology, Wuhan, 430070, China
[b] Sanya Science and Education Innovation Park of Wuhan University of Technology, Sanya, 572025, China

ARTICLE INFO

Article history:
Received 17 January 2025
Received in revised form
11 July 2025
Accepted 21 August 2025
Available online 26 December 2025

Keywords:
Flawed granite
Cyclic disturbance loading
Energy evolution
Fracture mechanism
Crack initiation angle

ABSTRACT

During geotechnical construction, flawed rock masses experience dynamic cyclic disturbances, leading to cumulative deformation and progressive damage. Consequently, elucidating the fracture mechanisms under cyclic loading is crucial for ensuring the safety and prolonged operation of deep underground engineering. This study investigated the mechanical responses of the surrounding rock at different locations by conducting triaxial tests on flawed granite using three distinct cyclic loading and unloading paths. Based on the maximum tangential stress criterion, a fracture mechanics model for open flaws was developed to analyze the intrinsic influence of confining pressure and flaw inclination on crack initiation behavior. The results indicate that graded unloading of confining pressure significantly weakens the flawed rock mass, reducing its peak stress to only 77.5 % of that observed under constant confining pressure. Conversely, flawed rock masses exhibit a substantial increase in bearing capacity under increasing graded cyclic loading, achieving a peak stress 19.3 % higher than that under cyclic disturbance loading. At a constant confining pressure of 40 MPa, the type of disturbance loading has no significant effect on the failure mode. The flawed granite specimens form a nearly V-shaped shear failure zone along the open flaw. However, confining pressure unloading induced a more complex shear-tensile composite failure mode in the specimens. The crack initiation angle increases nonlinearly with confining pressure, but decreases gradually as the flaw inclination angle (β) increases. These findings provide valuable insights for the safe construction of deep underground engineering.

1. Introduction

Weak structural planes are prevalent in deep rock masses due to tectonic movements. Their discrete distribution intensifies the inherent heterogeneity and anisotropy of the rock mass while weakening the mechanical properties of the rock mass. The spatial characteristics of non-persistent flaws critically govern the structural response of fractured rock masses under load disturbance, systematically influencing their mechanical properties and fracture behavior (Ma et al., 2019; Yang et al., 2019; Li et al., 2023; Haeri et al., 2024; Meng et al., 2024; West et al., 2024). Vibrational waves generated by tunnel excavation and other underground operations impose diverse low-frequency cyclic loads on both the surrounding rock and the excavation sections (Li et al., 2008; Yang et al., 2020). Under complex mechanical boundary conditions, the coupling effect of stress concentration and wave propagation leads to intricate stress paths, ambiguous damage mechanisms, and variable failure characteristics of flawed rock masses. Consequently, understanding the damage evolution process in rock masses with non-persistent flaws is essential. Equally important is the investigation of fracture mechanisms and the associated energy evolution characteristics. These insights provide a fundamental basis for evaluating the safety and stability of deep underground engineering subjected to combined dynamic-static loading disturbances.

In deep geotechnical engineering, the low-frequency cyclic disturbance loading represents a typical form of combined dynamic-static loading. Deep, flawed rock masses may exist in a critical stress state due to tectonic stress, making them highly responsive to external disturbances and exhibiting pronounced

* Corresponding author. School of Civil Engineering and Architecture, Wuhan University of Technology, Wuhan, 430070, China.
E-mail address: dingluyang7616@163.com (L. Ding).

Peer review under responsibility of Institute of Rock and Soil Mechanics, Chinese Academy of Sciences.

https://doi.org/10.1016/j.jrmge.2025.08.049

brittle behavior. Consequently, low-frequency cyclic disturbance loading can progressively accelerate damage accumulation in deep rock masses (Shi et al., 2022a; Chai et al., 2023; Wang et al., 2023a, b, 2024a). Yao et al. (2023) conducted a series of triaxial experiments to examine the combined effects of cyclic loading and the confining pressure release. The results showed that if the dynamic modulus decay rate in the first stage of cyclic loading exceeds 0.01, the rock fails in less than three cycles. Shi et al. (2022b) investigated the effect of cyclic loading on the failure modes and damage evolution of flawed rock masses through a series of multistage cyclic loading-unloading tests, as well as fatigue-creep tests. Their findings revealed that applying a creep load during fatigue loading enhances axial strength while decreasing axial deformation.

Energy evolution within the flawed rock mass reflects the overall damage process affecting the material (Su et al., 2018; Hu et al., 2020; Li et al., 2024a; Liang et al., 2024; Wang et al., 2024b). Microscopic failure initiates when the strain energy accumulated within the rock reaches the threshold required for crack formation, marking an initial phase in the damage evolution. As energy continues to accumulate and dissipate, the discrete distribution of microcracks gradually coalesces to form macrocracks, resulting in structural failure. This represents a later phase of damage evolution. Hu et al. (2020) studied the strain bursts triggered by high static pressures and cyclical disturbances. The findings revealed that periodic disturbances can significantly activate and accelerate rock damage. This energy-based failure mechanism can be collectively referred to as 'rock degradation through energy dissipation' due to the cyclic disturbance. Liu et al. (2016) quantified the degree of initial compaction via compaction coefficients and established a recursive damage constitutive model based on uniaxial cyclic loading energy dissipation. Liu and Liu (2017) performed triaxial disturbance loading experiments on rock-like materials with a persistent flaw. It was found that both confining pressure and inclination angle of the flaw significantly affect the dynamic deformation and failure mechanisms of the specimens. As a quantifiable parameter for characterizing the strength of the stress field at the tip of a flaw, the stress intensity factor has been widely used by many scholars to study the fracture mechanics of flawed rock masses under different stress conditions (Tang et al., 2023; Cui et al., 2024). Melin (1986) concluded that shear cracks are more likely to be initiated with increasing confining pressure or with a decreasing ratio between the critical stress intensity factors. Zhou and Liu (2023) analyzed the stress intensity factor K_I under compressive loading based on Muskhelishvili's tensile stress hypothesis (Goss, 1964) and further investigated the fracture mechanisms of water-bearing flawed rock masses.

The excavation process in deep geotechnical engineering is multistage. Frequent blasting and unloading activities induce cumulative damage to the surrounding rock at various locations (Zhang and Zhao, 2014; Hu et al., 2018; Liu et al., 2019), as illustrated in Fig. 1. Type-I disturbance loading refers to cyclic loading, which is commonly employed to examine the disturbance effect of construction-induced vibrational wave on the far-field surrounding rock masses (Zhong et al., 2022; Xu et al., 2023; Chen et al., 2024; Jiang et al., 2024); Type-II disturbance loading combines cyclic loading and confining pressure grade unloading, considering the multistage confining pressure unloading path experienced by the rock mass near the palm face during excavation of underground engineering (Wang et al., 2023b). Type-III disturbance loading refers to the graded increasing cyclic loading. Variations in the position of the vibration source over a finite distance cause fluctuations in the amplitude of the disturbance loads on the flaw mass. Therefore, type-III disturbance loading can be used to characterize the multistage damage to the rock mass induced by frequent blasting (Xiao et al., 2020; Wang et al., 2022; Liu et al., 2024a; Ran et al., 2024).

With the progressive advancement in deep tunnel excavation, disturbance-induced damage in the surrounding rock exhibits distinct spatiotemporal variability. Stress conditions and types of disturbance loading vary significantly across different locations within the surrounding rock. Several studies have examined excavation unloading effects on rock mass stability under complex geological conditions (Xing et al., 2018; Lin et al., 2020; Hou et al., 2023). However, most existing research tends to focus on single factors, such as variations in confining pressure or individual disturbance types (Gong et al., 2022; Zhang et al., 2024). While these studies have advanced the understanding of specific failure mechanisms, they remain insufficient to fully capture the complex failure processes occurring in deep underground excavations. A more comprehensive investigation is required to reveal the progressive failure mechanisms more holistically. Such an investigation should simultaneously consider the effects of dynamic loading, in situ stress conditions, and the coalescence of pre-existing flaws. The present study employed an improved triaxial loading system to investigate the mechanical behavior and failure mechanisms of granite with a non-persistent flaw. The investigation took into account the stress conditions of the surrounding rock in deep tunnels and incorporated three types of cyclic disturbance loading (cyclic loading (Type-I), cyclic loading and confining pressure grade unloading (Type-II), and graded increasing cyclic loading (Type-III)). The complete process of energy evolution and energy release characteristics of the flawed rock mass was discussed based on thermodynamic principles. The maximum tangential stress (MTS) criterion was employed to develop an open-flaw fracture mechanics model, elucidating the intrinsic response mechanism of the crack initiation behavior to the confining pressure and flaw inclination angle. Furthermore, the mechanism of localized nucleation failure under passive confinement was analyzed. Based on the findings, a method for disaster prevention and mitigation in deep underground engineering was proposed.

2. Experimental methodology

2.1. Specimens and experimental system

The granite specimens were sourced from the underground powerhouse of Shuangjiangkou Hydropower Station in China. The in situ rock mass burial depth was approximately 400 m. Hydraulic fracturing tests measured a maximum principal stress of 38 MPa. To minimize the test bias, all specimens were obtained from the same rock block to ensure that the mineral composition of the specimens was consistent. The mineral phases and microstructure of granite were analyzed using microscopic testing methods. The test results are shown in Fig. 2b and c. Dominant mineral components include quartz, biotite, microcline, albite, and chlorite. Feldspars dominate the composition (54.3 %), with quartz and biotite contributing 16.8 % and 20.4 %, respectively. The scanning electron microscopy (SEM) results reveal a discrete distribution of microcracks and micropores within the granite. The International Society for Rock Mechanics (ISRM) recommends that specimens should be cylindrical in shape with a diameter of 50 mm and a height-diameter ratio of 2:1. The non-parallelism of the machined end faces must be less than 0.05 mm. Ultimately, non-persistent flaws with a length of 30 mm and a width of 0.4 mm were prefabricated from intact specimens via the wire-cutting technology (as shown in Fig. 2a). Highly uniform specimens (i.e. precisely drilled) with good-quality flaws were selected for testing. According to the research results of Gong et al. (2022), it is known that the propagation paths of coplanar cracks in rock masses with

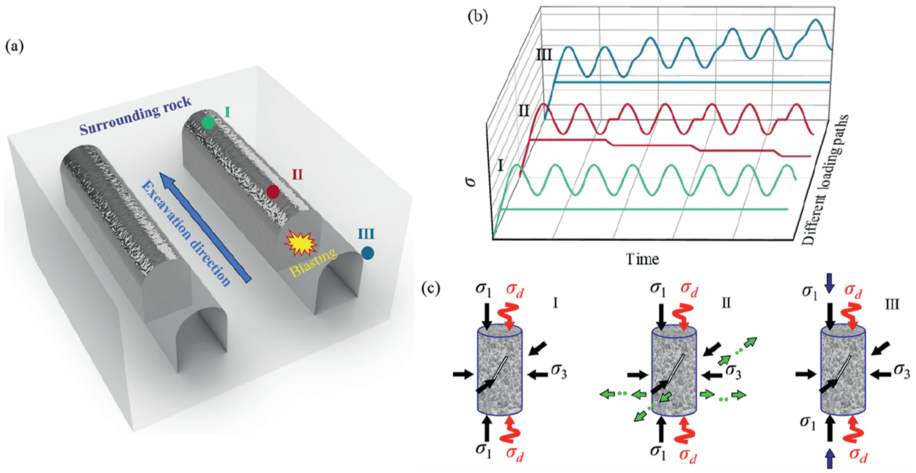

Fig. 1. Schematic diagram of deep rock stress models (revised after Liu et al., 2019): (a) Schematic of the underground cavern; (b) Schematic of different loading paths; (c) Stress schematic of rock masses, where σ_1 is the axial pressure, σ_3 is the confining pressure, and σ_d is the disturbance loading.

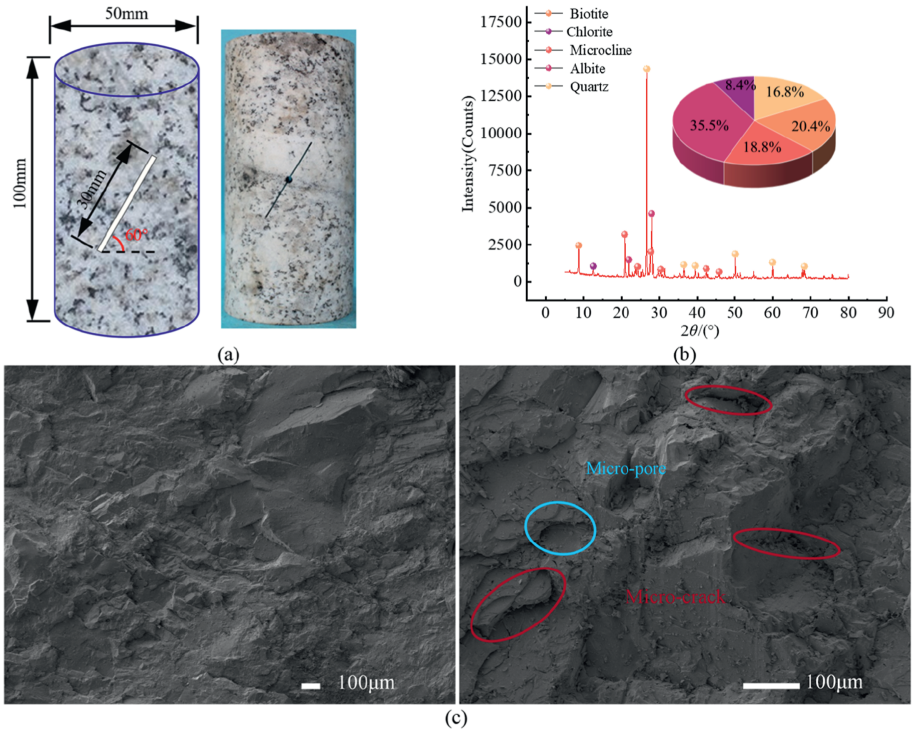

Fig. 2. Prefabricated granite specimen with a single flaw and microstructure information (a) Prefabricated specimen with a single flaw; (b) XRD test result; and (c) SEM results for granite.

a non-persistent flaw at 60° inclination under triaxial compression are almost exactly coincident with the flaw inclination. This results in the lowest peak strength compared to other flaw inclination conditions. Therefore, a 60° inclination angle was selected as one of the fundamental operating conditions in this study. The mechanical parameters of the granite specimen with a flaw inclination of 60° are summarized in Table 1 (Liu et al., 2024b).

The tests were conducted on a servo-assisted hydraulic material testing machine (MTS 795). The device has a maximum axial load capacity of 2750 kN, a maximum confining pressure of 120 MPa, and a maximum fatigue load of 2500 kN. It allows strain rates ranging from 10^{-6} s^{-1} to 10^{-1} s^{-1} during loading and unloading, and fatigue frequencies from 0 Hz to 70 Hz.

2.2. Test procedure

As shown in Fig. 3, different types of cyclic disturbance loading tests were carried out in three stages. Stage I (*OA*) and stage II (*BC*) represent conventional triaxial test loading paths, whereas stage III (*CN*) corresponds to the disturbance loading path. In Stage I, the confining pressure was elevated to 40 MPa at a rate of 0.05 MPa/s via the stress control system. In Stage II, axial pressure was applied to 85 % of the mean peak stress by the displacement control system at a rate of 0.002 mm/s (point *C* in Fig. 3). With increasing distance from the explosion source, the detonation wave attenuates rapidly and propagates through the rock mass as seismic waves (Ma et al., 2020). Additionally, the findings of several studies indicate that

Table 1
Basic mechanical parameters of the granite specimen with a flaw inclination of 60°.

Property	Value
Density, ρ (kg/m^3)	2550
P-wave velocity, V_p (m/s)	3996
Young's modulus, E_s (GPa)	28.01
Poission's ratio, μ	0.22
Triaxial peak strength, $\sigma_1 - \sigma_3$ (MPa)	239.63

when the disturbance frequency is 5 Hz and the amplitude is 0.03 mm, both the peak strength and axial strain of the rock specimen reach critical thresholds (Liu et al., 2024b). This frequency aligns with the low-frequency characteristics of mine microseismic activity (Chen et al., 2025). Consequently, a disturbance frequency of 5 Hz and an amplitude of 0.03 mm were selected as the disturbance parameters for this study. The loading paths for different types of disturbance loading vary during Stage III. For cyclic loading disturbance (type-I), a sinusoidal disturbance load with a frequency of 5 Hz and an amplitude (D_v) of 0.03 mm was applied in the axial direction until specimen failure. For cyclic loading and confining pressure grade unloading (type-II), the applied confining pressure was decreased at a constant rate of 0.2 MPa/s until it reached the value of 30 MPa. This allows for the investigation of brittle fracture characteristics induced by confining pressure unloading (Wang et al., 2020; Guo et al., 2021). The confining pressure was maintained at this value for 500 cycles of the cyclic disturbance. It was then further reduced, and the process was repeated until the specimen failed. For graded increasing cyclic loading disturbance (type-III), 500 cycles of sinusoidal disturbance loading were applied first. The axial displacement was then increased by 0.06 mm, and the process of cyclic loading and stress increment was repeated until specimen failure.

3. Mechanical behavior

3.1. Deviatoric stress–strain response

Fig. 4a–c presents the deviatoric stress–strain curves of flawed granites under various disturbing loads. In these plots, $\sigma_1 - \sigma_3$ is the deviatoric stress, ε_1 is the axial strain, and ε_3 is the radial strain. Several studies classify failure stages by identifying whether the specimen has cracked, with the stress corresponding to a crack volume strain of zero being referred to as the crack initiation stress (Li et al., 2024b; Xing et al., 2024). In studies on flawed rock masses under high confining pressure, it has been observed that the radial strain remains unchanged during the initial loading stage (Shan et al., 2021; Chang et al., 2022). However, the epistemic significance of this deformation mechanism has not been contextualized. In particular, its role within the framework of the mutual characterization of mechanical properties and fracture behavior in flawed rock masses remains insufficiently explored. A comparative analysis of the axial and radial stress–strain curves reveals that the mechanical properties of the granite specimens can be categorized into three stages: the axial deformation stage (only axial deformation occurs), the crack development stage (rapid generation of microcracks), and the sliding mode fracture stage (microcracks coalesce and stress decreases). Fig. 4d illustrates the distribution of characteristic parameters of flawed rock masses under varying disturbance loads.

The deviatoric stress–axial strain curves of the flawed rock mass under type-I disturbance loading exhibit a linear growth trend during the preloading process, with no significant radial deformation occurring. This indicates that only axial deformation takes place in the rock specimen at this stage. The prefabricated open flaw undergoes compression, and the specimen remains in the axial deformation stage. As shown in Fig. 4a, when the deviatoric stress exceeds 150 MPa, the deviatoric stress–axial

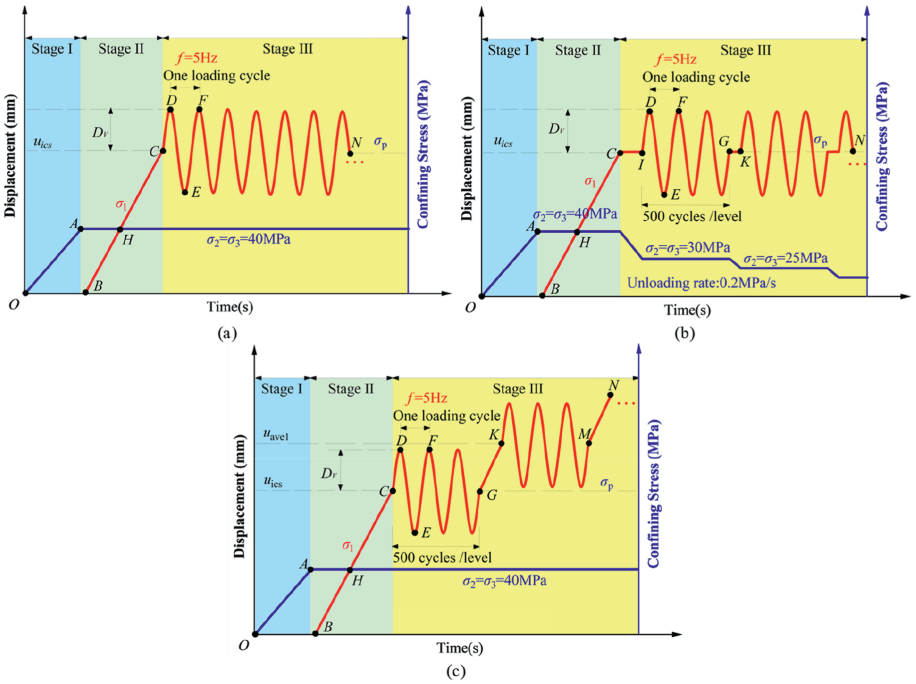

Fig. 3. Loading paths diagram: (a) Cyclic loading disturbance; (b) Cyclic loading and confining pressure grade unloading disturbance; and (c) Graded increasing cyclic loading disturbance.

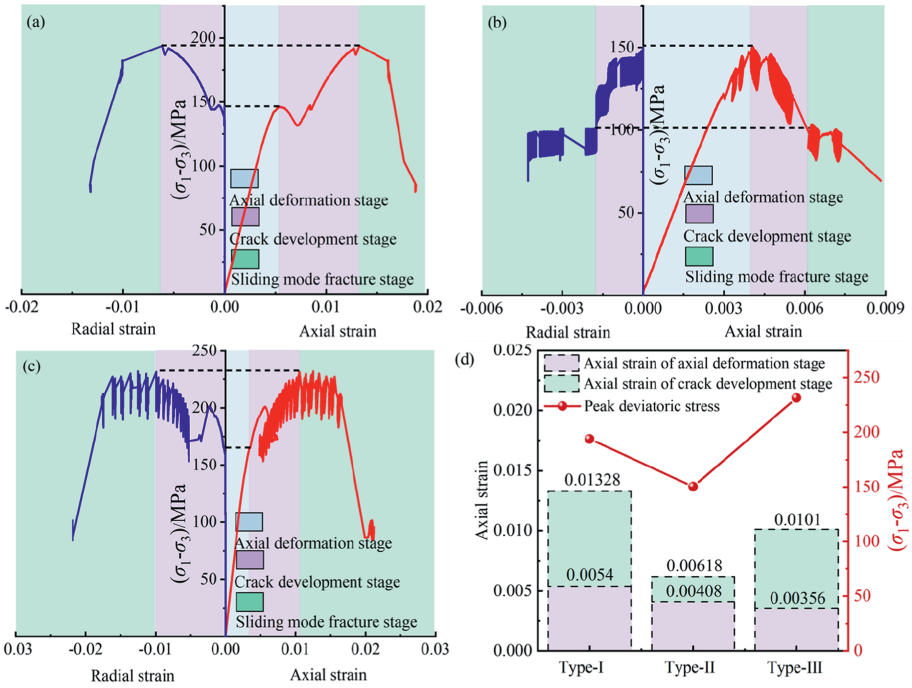

Fig. 4. Deviatoric stress–strain curves: (a) Type-I disturbance loading; (b) Type-II disturbance loading; (c) Type-III disturbance loading; and (d) Statistical chart of stress–strain eigenvalues.

strain curve declines, and the radial strain gradually increases. It is considered that the open flaw is completely compressed to closure. The resulting anti-wing crack extends to the end of the specimen, nearly forming a penetration failure. This process generates significant axial displacement but induces minimal radial strain. At this point, the damage pattern of the rock specimen has transitioned to the stage of coplanar crack development. With continued cyclic loading, coplanar cracks are discretely initiated and gradually coalesce. The maximum disturbance load limit also decreases, signaling the entry of the rock specimen into the sliding mode fracture stage. When the coplanar crack propagates from the tip of the flaw to the end of the specimen, the stress in the rock specimen drops abruptly, indicating structural failure. These test results demonstrate that continuous disturbance loading causes cumulative fatigue damage in the flawed rock mass as it approaches ultimate stress equilibrium.

The deviatoric stress–strain curves of the flawed rock specimens under type-II disturbance loading are shown in Fig. 4b. According to the loading path presented in Fig. 3b, the confining pressure was first reduced to 30 MPa prior to disturbance loading. During the subsequent disturbance loading, the confining pressure was released in a graded manner. As a result, the peak strength of the flawed rock specimens under this condition is significantly lower than that under pure cyclic loading. The test results indicate that when the deviatoric stress reaches 150 MPa under cyclic disturbance, the radial strain begins to increase, marking the onset of the coplanar crack development stage. As the confining pressure decreases further, the rate of coplanar crack initiation and propagation is notably accelerated. The microdamage of the rock specimen accumulates rapidly. Observing the deviatoric stress–radial strain curve, it is found that the deviatoric stress decreases to 125 MPa with an obvious drop phenomenon, while axial strain increases substantially. This suggests that the flawed rock mass has entered the stage of slip mode fracture. With the gradual reduction of the confining pressure to 0 MPa, both axial and radial strains increase rapidly until the flawed rock specimen loses its bearing capacity. These observations highlight the significant effect of confining pressure on the mechanical properties of the rock material. Even under low confining pressures, the specimens exhibit pronounced ductile characteristics.

As shown in Fig. 4c, when the deviatoric stress reaches 165 MPa, the open flaw is compressed to closure, accompanied by an increase in radial strain, marking the onset of the crack development stage. The mechanical properties improve under graded increasing cyclic disturbance loading. The stress in the flawed rock mass progressively increases with graded increasing cyclic disturbance loads, accompanied by the continuous accumulation of microdamage. During the slip mode fracture stage, the deviatoric stress is maintained between 190 MPa and 230 MPa. It is observed that the stress hysteresis curve is more densely distributed before the peak deviatoric stress is reached in the flawed rock specimens, while it gradually becomes sparse after the peak. This suggests that strain softening occurs after the yield strength of the flawed rock mass is reached under cyclic disturbance loading. During this stage, cracks gradually coalesce until penetration occurs, triggering an abrupt stress drop and instantaneous structural failure.

Comparing the characteristic curves of the mechanical properties under the three loading paths, it is evident that a stable axial deformation phase exists in the initial loading stage. Strain softening occurs in all post-peak stages, exhibiting ductile failure characteristics. This is a common feature of flawed rock masses under triaxial compression (Shan et al., 2021; Chang et al., 2022).

The stress–strain relationship reflects the mechanical properties and constitutive behavior of the rock specimens under triaxial loading. As shown in Fig. 4d, the strain of the flawed rock specimens under type-II disturbance loading is smaller than that under type-I disturbance loading. This indicates that graded unloading of the confining pressure under the same cyclic loading leads to the weakening of the flawed rock mass, as evidenced by a significant reduction in the peak stress. Due to elastoplastic constitutive properties and strain softening, the rock specimens exhibit the

stress drop phenomenon earlier. Lower peak stress and peak strain indicate that the degree of damage to the rock specimen is much lower than that under pure cyclic disturbance loading. Furthermore, it was observed that the deviatoric stress–radial strain curves exhibited a staged creep characteristic during the graded unloading of the confining pressure. This indirectly indicates that during the crack development and slip fracture stage, fatigue stress causes continuous accumulation of microdamage in the flawed rock mass. According to Fig. 4d, it is found that under the same confining pressure, the graded increasing cyclic loading resulted in a significant increase in the stress level of the rock specimens. The strain corresponding to the peak stress is smaller. This indicates that the graded increasing cyclic loading improves the efficiency of damage accumulation. It is worth noting that under type-I and type-III disturbance loading, the axial strain is consistent (about 0.016) in the sliding mode fracture stage when the failure of the flawed rock mass undergoes instability. However, the radial strains differ significantly, being −0.01 and −0.017, respectively. It indicates that the damage caused by graded increasing cyclic loading is greater than that caused by cyclic loading alone. This is primarily reflected in the radial displacement of rock specimens, indicating a more significant degree of slip failure. Under constant confining pressure, the coordinated deformation of the rock specimens resulted in a clearer symmetry between the stress–radial strain curve and the stress–axial strain curve following the axial deformation stage. This behavior contrasts markedly with that observed under type-II disturbance loading.

3.2. Deformation characteristics

According to the mechanics of materials and elasticity, the volumetric strain of a material under compressive loading can be defined as (Li et al., 2012):

$$\varepsilon_v = (V - V_0) / V_0 \tag{1}$$

where V_0 and V represent the material volume before and after deformation, respectively. According to the intrinsic characteristics of volumetric strain that only considers normal strain, the volumetric strain of cylindrical specimens can be calculated using the following formula:

$$\varepsilon_v = (1+\varepsilon_3)^2(1+\varepsilon_1) - 1 \tag{2}$$

To comprehensively discuss the deformation characteristics of the flawed rock mass under different types of disturbance loading, the strain–time curves shown in Fig. 5 are plotted in conjunction with Eq. (2), where ε_{vp}, ε_{vz}, and ε_{vf} are the peak value, zero point, and final values of volumetric strain, respectively. Different from the general rock volumetric strain–time curves, in the present study, $t = 0$ s corresponds to the stress state of the point H in loading stage II (Fig. 3), at which $\sigma_1 = \sigma_2 = \sigma_3 = 40$ MPa. As a result, the strain–time curves do not exhibit the phase of microcrack closure and volume contraction within the rock at the initial stage of triaxial loading. Consequently, the volumetric strain is not negative at the initial stage of loading. Due to the unique fracture mechanism of the rock mass with an open flaw under triaxial compression, the radial strain remains constant throughout the preloading process. According to Eq. (2), ε_v and ε_1 are consistent at this stage.

When radial deformation occurs, an eigenvalue ε_{vp} is observed in the volumetric strain–time curve, and the volumetric strain continues to decrease as radial strain increases. According to Eq. (2), there is a specific relationship between the axial and circumferential coordinated deformations of the flawed rock mass under triaxial compression. ε_3 can be expressed as a function of ε_1 as

$$\varepsilon_3 = f(\varepsilon_1) \quad (\varepsilon_3 < 0) \tag{3}$$

Eq. (2) can be expressed as

$$F(\varepsilon_1) = \begin{cases} (1+\varepsilon_1) - 1 & (f(\varepsilon_1) = 0) \\ [1+f(\varepsilon_1)]^2(1+\varepsilon_1) - 1 & (f(\varepsilon_1) < 0) \end{cases} \tag{4}$$

As shown in Fig. 5, it is found that $\varepsilon_1 = \varepsilon_s$, which leads to

$$\left.\begin{array}{l} F'(\varepsilon_s) = 0 \\ f(\varepsilon_s) \to 0^- \end{array}\right\} \tag{5}$$

where ε_s is the eigenvalue of axial strain.

Based on Eq. (4), the following equation can be obtained:

$$\frac{dF(\varepsilon_1)}{d\varepsilon_1} = 2\frac{df(\varepsilon_1)}{d\varepsilon_1}(1+f(\varepsilon_1))(1+\varepsilon_1) + (1+f(\varepsilon_1))^2 \tag{6}$$

Substituting Eq. (5) into Eq. (6), the following equation is obtained:

$$f'(\varepsilon_s) = \frac{-1}{2(1+\varepsilon_s)} \tag{7}$$

In the present test, the observed value of ε_s is less than 0.01. Therefore, it is considered that $f'(\varepsilon_s)$ is approximately −0.5. The intrinsic relationship between axial and radial strains in the flawed rock mass under triaxial disturbance loading is demonstrated through the eigenvalues of volumetric strains. This behavior reflects the passive coordinated deformation of the flawed rock mass under external loads.

It is observed that the volumetric strain takes the longest time to reach the characteristic value of ε_{vp} under type-II disturbance loading. Considering the low confining pressure, the early cyclic disturbance loading caused the rock specimen to develop cyclic strains in the axial direction, mainly driven by elastic deformation. The graded unloading of confining pressure further reduced the bearing capacity of the flawed rock specimens and led to the accumulation of radial strains. The volumetric strain reaches its peak when the open flaw is compressed to closure.

The transition of volumetric strain to zero (ε_{vz}) signifies departure from shear dilatation and indicates advanced damage accumulation. Both axial and radial strains experience substantial variations when the volumetric strain reduces to zero under different types of disturbance loading. Type-III disturbance loading achieves ε_{vz} most rapidly, demonstrating significantly higher damage accumulation efficiency than type-I disturbance loading. Conversely, type-II disturbance loading requires the greatest cycle count and duration to reach ε_{vz}. This indicates that the confining pressure conditions have a significant effect on the damage accumulation efficiency of flawed rock masses. Specifically, low confining pressure substantially diminishes damage efficiency. Furthermore, due to the lower stress level in the rock specimen, the ultimate damage under type-II disturbance loading is less than that under other types of disturbance loading. As established by Eq. (1), the volume of the rock specimen decreases when ε_v is negative. As shown in Fig. 5, volume decrease occurs immediately before instability failure in the flawed rock specimens under type-I and type-III load disturbances. In contrast, the volumetric strain of the rock specimens under type-II disturbance loading drops abruptly below zero only as instability failure approaches. This indicates that the fracture mechanism and failure path of the flawed rock mass under type-II disturbance loading are distinct from those under other loading regimes.

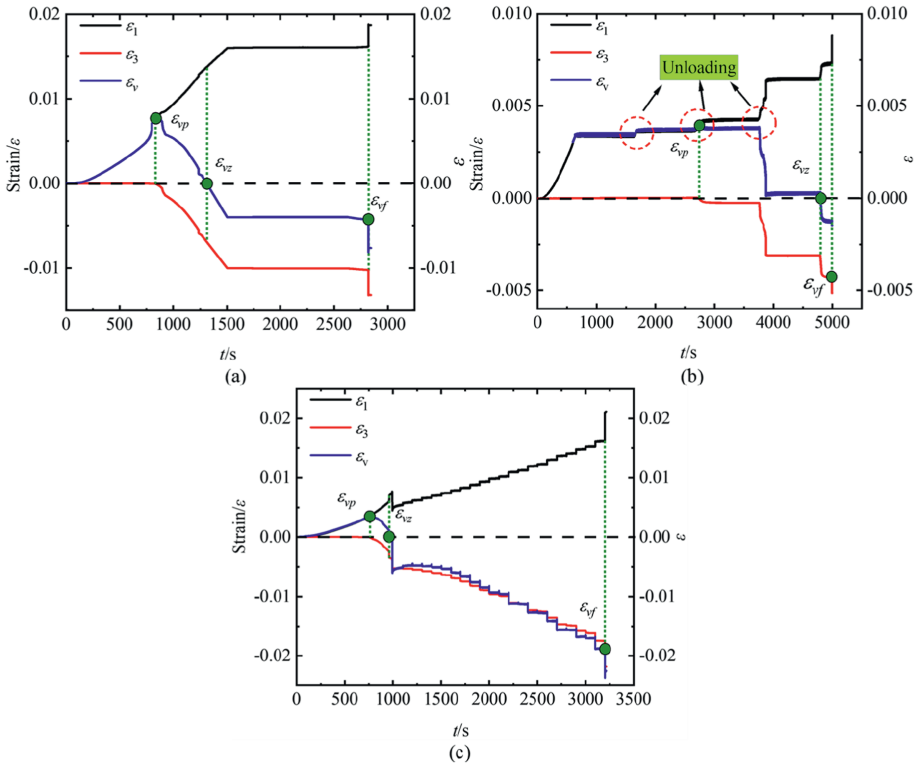

Fig. 5. Strain–time curves under different types of disturbance loading: (a) Type-I disturbance loading; (b) Type-II disturbance loading; and (c) Type-III disturbance loading.

3.3. Fracture behavior analysis

The crack initiation angle of a flawed rock mass is a crucial factor in determining its ultimate fracture mode. This angle dictates the propagation trajectories of macroscopic cracks under stable mechanical conditions (Chang et al., 2022). A schematic diagram of the loading process on a rock specimen with a prefabricated open flaw is shown in Fig. 6a. Corresponding load distributions across the open flaw surface are detailed in Fig. 6b.

In Fig. 6, σ_N and τ_f represent the normal and shear stress distributed on the flaw surface, respectively, and their expressions are as follows (Yang et al., 2021; Zhou and Liu, 2023):

$$\sigma_N = \frac{1}{2}(\sigma_1 + \sigma_3) - \frac{1}{2}(\sigma_1 - \sigma_3)\cos(2\beta) \tag{8}$$

$$\tau_f = \frac{1}{2}(\sigma_1 - \sigma_3)\sin(2\beta) \tag{9}$$

where β is the angle between the prefabricated open flaw and the direction of maximum principal stress applied. The stress intensity factor at the tips of the flaw can be calculated by (Irwin, 1957):

$$K_I = Y\sigma_N\sqrt{\pi a} \tag{10}$$

$$K_{II} = Y\tau_f\sqrt{\pi a} \tag{11}$$

$$Y = \sqrt{\frac{D}{\pi a \sin\beta}\tan\frac{\pi a \sin\beta}{D}} \tag{12}$$

where K_I and K_{II} are the stress intensity factors in modes I and II,

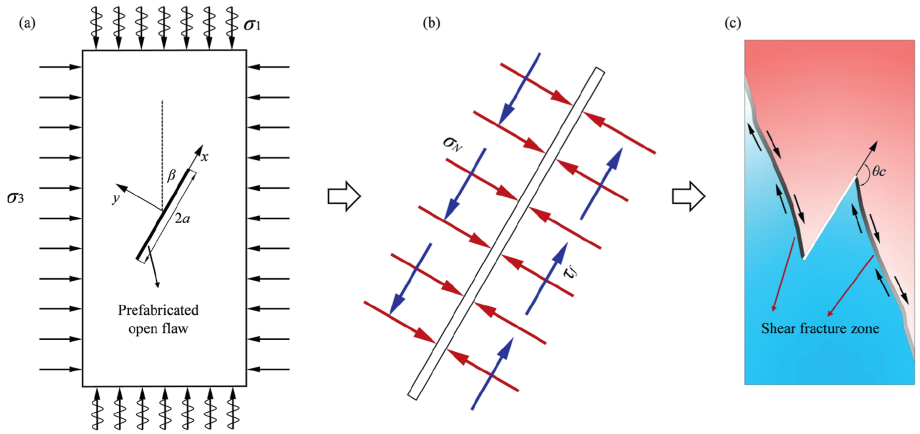

Fig. 6. Stress and fracture analysis diagram of a specimen: (a) Loading method; (b) Stress distribution at the flaw surface; and (c) Fracture behavior.

respectively; Y is the boundary correction factor, which is taken as 1.2085 in this study; and D and a represent the specimen diameter and the half-length of the flaw, respectively.

The stress field at the tip of the flaw, considering T-stress, is defined in polar coordinates as (Tang, 2015):

$$\left.\begin{aligned}\sigma_r &= \frac{1}{2\sqrt{2\pi a}}K_{\mathrm{I}}\sin\frac{\theta}{2}(3\cos\theta-1)+\frac{1}{2\sqrt{2\pi a}}K_{\mathrm{II}}\sin\frac{\theta}{2}(3\cos\theta-1)\\ &+T_x\cos^2\theta+T_y\sin^2\theta\\ \sigma_\theta &= -\frac{1}{2\sqrt{2\pi a}}\cos\frac{\theta}{2}[K_{\mathrm{I}}(1+\cos\theta)-3K_{\mathrm{II}}\sin\theta]+T_x\sin^2\theta\\ &+T_y\cos^2\theta\\ \tau_{r\theta} &= \frac{1}{2\sqrt{2\pi a}}\cos\frac{\theta}{2}[K_{\mathrm{I}}\sin\theta+K_{\mathrm{II}}(3\cos\theta-1)]\\ &-(T_x-T_y)\sin\theta\cos\theta\end{aligned}\right\} \tag{13}$$

where T_x and T_y are the parallel and perpendicular non-singular stresses in the vicinity of the flaw tip, respectively. Under triaxial compression, T_x and T_y can be expressed as

$$\left.\begin{aligned}T_x &= \sigma_1\cos^2\beta+\sigma_3\sin^2\beta\\ T_y &= \sigma_1\sin^2\beta+\sigma_3\cos^2\beta\end{aligned}\right\} \tag{14}$$

According to the MTS criterion, when crack initiation occurs, the condition can be stated as

$$\frac{\partial\sigma_\theta}{\partial\theta}=0,\frac{\partial^2\sigma_\theta}{\partial\theta^2}<0 \tag{15}$$

It is worth noting that normally, when discussing the crack initiation angle for closed flaws under triaxial loading, cracks are typically assumed to initiate under pure mode II loading on the flaw surface. In the classic MTS criterion, the crack initiation angle θ_c is a constant value that equals 70.5° in pure mode II loading. For open flaws, the flaw surface is subjected to a combination of normal and shear stresses. Initial cracks with mixed-mode character are formed under mixed-mode (mode I-II) loading. Substituting Eq. (13) into Eq. (15) shows that the θ_c needs to satisfy the following formulas:

$$\left.\begin{aligned}-\frac{3}{4\sqrt{2\pi a}}\cos\frac{\theta_c}{2}[K_{\mathrm{I}}\sin\theta_c+K_{\mathrm{II}}(3\cos\theta_c-1)]\\ +2(T_x-T_y)\sin\theta_c\cos\theta_c=0\\ -\frac{3}{8\sqrt{2\pi a}}\sin\frac{\theta_c}{2}[K_{\mathrm{I}}\sin\theta_c+K_{\mathrm{II}}(3\cos\theta_c-1)]\\ -\frac{3}{4\sqrt{2\pi a}}\cos\frac{\theta_c}{2}[K_{\mathrm{I}}\cos\theta_c-3K_{\mathrm{II}}\sin\theta_c]\\ +2(T_x-T_y)\cos(2\theta_c)<0\end{aligned}\right\} \tag{16}$$

This indicates that the crack initiation angle of an open flaw depends on flaw inclination β, crack initiation stress σ_c, and confining pressure σ_3. For granite specimens with 60° non-persistent flaws under a confining pressure of 40 MPa, Liu et al. (2024b) determined the initiation stress to be 135 MPa using the crack volumetric strain method. Substituting this value into Eq. (16) yields $\theta_c = -129°$. This prediction aligns with experimental observations. Two-dimensional (2D) models typically assume plane stress or plane strain conditions, whereas cylindrical specimens exhibit axisymmetric three-dimensional (3D) geometric characteristics, resulting in a more complex stress distribution. The cylindrical curvature induces local stress concentrations and a triaxial stress state, potentially introducing errors in the calculation of the stress intensity factor. Additionally, experimental uncertainties may further affect the accuracy of the results. However, considering the boundary correction factor helps to minimize these errors.

It is considered that, during the axial deformation stage, the flawed rock specimen undergoes displacement deformation, as illustrated in Fig. 6c. The volumetric dilatation caused by the fracture surfaces remains unrepresented in the radial strain under confining pressure. Based on the deformation behavior of the flawed rock specimens, the volume of the open flaw continuously decreases until closure. It is worth noting that the stress state on the flaw surface shifts notably following the closure of the prefabricated flaw. The shear stress becomes the controlling factor for the subsequent failure behavior originating from the crack surface. The internal stress state of the rock mass is conducive to the initiation of coplanar cracks. Progressive loading drives the coalescence of discrete coplanar cracks, resulting in penetration failure along the tangential direction of the flaw.

The ultimate failure patterns of the flawed rock masses under distinct disturbance loadings are shown in Fig. 7. The specimens exhibit similar failure states under cyclic loading (Fig. 7a) and graded increasing cyclic loading (Fig. 7c). During the preloading period, anti-wing cracks continued to propagate from the tips of the flaw to the end of the specimen. The prefabricated open flaw was compressed to closure when the deviatoric stress reached 150 MPa. Subsequently, coplanar cracks coalesced and penetrated, resulting in an increase in radial strain. The coplanar cracks were found to have a straight orientation under cyclic loading, whereas their direction was variable under graded increasing cyclic loading. This suggests that the disturbance amplitude of the load has a significant effect on coplanar crack propagation behavior. During testing, a distinct rupture sound was heard when the specimen ultimately failed. This is consistent with the fracture behavior characterized by the deviatoric stress–strain curve. Although the specimen exhibits ductile characteristics upon entering the sliding mode fracture stage, it still retains the inherent brittleness of rock, leading to instantaneous instability failure. As shown in Fig. 7b, the flawed rock specimens exhibited fundamentally different failure modes under type-II disturbance loading. During the preloading stage, owing to the typical fracture behavior of flawed rock masses under triaxial compression, anti-wing cracks developed at the tips of the open flaw. However, the specimen strength progressively declined due to the unloading effect of the confining pressure. As a result, the discretely distributed coplanar cracks along the tangential direction of the flaw failed to coalesce. Instead, wing cracks propagated symmetrically from the ends of the flaw. Wing cracks are typically generated through a tensile fracture mechanism, which is distinct from the shear-dominated mechanism responsible for the formation of coplanar cracks (Modiriasari et al., 2017). This indicates that, compared to cyclic loading, the confining pressure is the determining factor for the failure mode of the flawed rock mass.

In summary, deep geotechnical engineering is significantly influenced by complex tectonic stress fields. Shear-induced anti-wing cracking constitutes the foundational fracture mode under construction-induced disturbances. Coplanar and wing cracking will not occur independently as complementary paths for stress release. Under type-I and type-III disturbance loading, the specimens exhibit an axially symmetric nearly V-shaped damage pattern along the open flaw, with shear failure as the dominant failure mode. In contrast, the failure mode under type-II disturbance loading is characterized by a mixed shear-tensile failure.

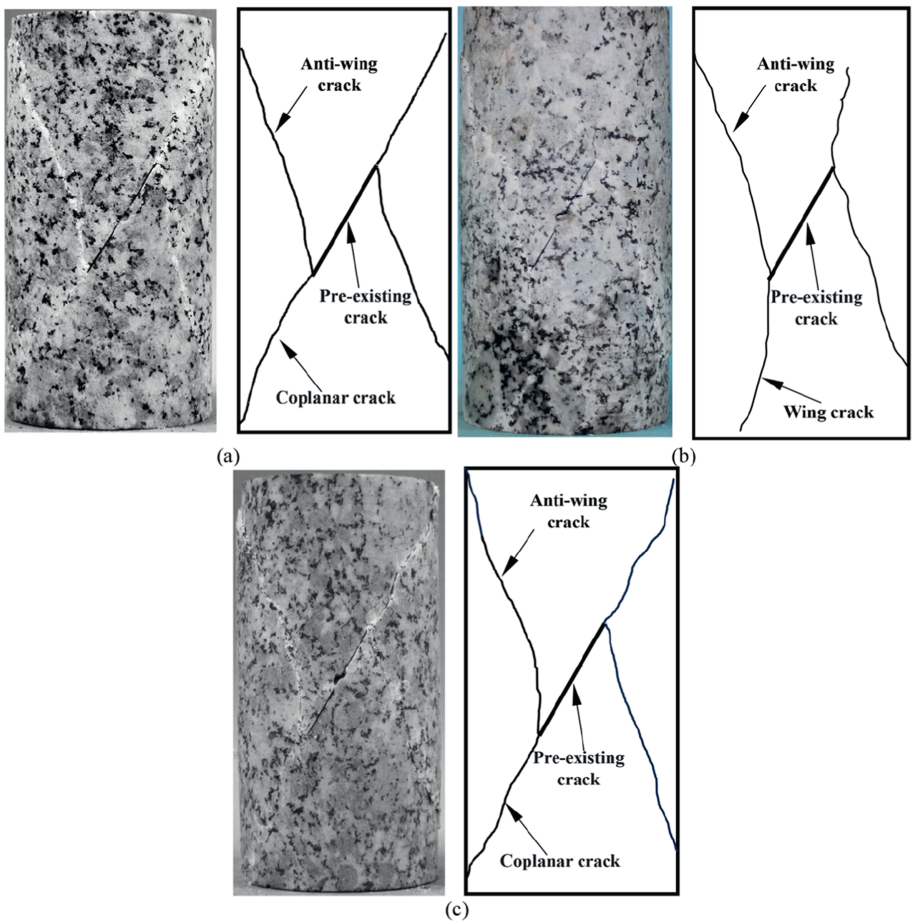

Fig. 7. Ultimate failure modes of test specimens under different disturbance loadings: (a) Type-I disturbance loading; (b) Type-II disturbance loading; and (c) Type-III disturbance loading.

4. Energy evolution and dissipation mechanisms

4.1. Energy evolution behavior

Failure of flawed rock masses initiates with microcracking at flaw tips, progresses through coalescence into localized damage, and culminates in structural instability. From the perspective of energy evolution, the nature of the rock triaxial dynamic-static disturbance loading test can be viewed as an energy accumulation process accompanied by trace dissipation until the energy is fully dissipated and released. According to thermodynamic principles (Peng et al., 2015; Liu et al., 2024a; Wang et al., 2024c), the energy input into the rock specimen can be calculated by

$$U = U_e + U_d \tag{17}$$

where U is the total energy, U_e is the elastic strain energy, and U_d is the dissipated energy.

Unlike the relatively simple process of continuous energy accumulation under monotonic loading, the efficiency of energy accumulation under cyclic disturbance loading is significantly lower than that under monotonic loading conditions. Fig. 8 shows a schematic diagram depicting the loading paths within a single cycle, where *ABC* represents the loading path associated with strain. The energy density can be calculated by integrating the stress–strain curve. The input energy corresponding to unit strain during loading is represented by the area of the region $EF\varepsilon_{i+1}\varepsilon_i$. Similarly, the input energy corresponding to unit strain during unloading is represented by the area of the region $fe\varepsilon_i\varepsilon_{i+1}$. The area enclosed by the hysteresis loop of the stress–strain curve represents the net energy input per cycle.

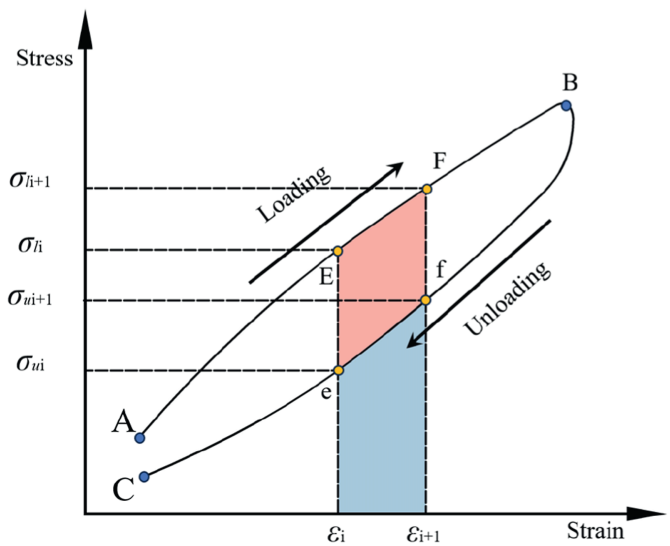

Fig. 8. Load path diagrams for single-cycle loading.

By summing the area of a tiny trapezoid according to the

concept of the definite integral, the energy density can be calculated as (Xie et al., 2005):

$$u = u_1 + u_3 \tag{18}$$

$$u_1 = \int \sigma_1 \mathrm{d}\varepsilon_1 = \sum_{i=0}^{n} \frac{1}{2}(\varepsilon_{i+1} - \varepsilon_i)_1(\sigma_{i+1} - \sigma_i)_1 \tag{19}$$

$$u_3 = 2\int \sigma_3 \mathrm{d}\varepsilon_3 = \sum_{i=0}^{n} \frac{1}{2}(\varepsilon_{i+1} - \varepsilon_i)_3(\sigma_{i+1} - \sigma_i)_3 \tag{20}$$

$$u_e = \frac{1}{2E_t}\left[\sigma_1^2 + 2\sigma_3^2 - 2\nu_t\left(2\sigma_1\sigma_2 + \sigma_3^2\right)\right] \tag{21}$$

where u_1 and u_3 are the axial and radial total strain energy densities, respectively; E_t and ν_t represent the elastic modulus and Poisson's ratio of the specimen at time t, respectively, during the loading and unloading process; ε_i and ε_{i+1} are the radial strains corresponding to the integration step, respectively; and σ_i and σ_{i+1} are the confining pressures corresponding to the integration step, respectively.

The energy evolution during the test was calculated using the stress–strain data recorded during the triaxial test and Eqs. (17)–(21), as shown in Fig. 9. Based on the energy accumulation and dissipation processes under different disturbance loadings, the energy evolution can be divided into four stages: Stage I (elastic strain energy accumulation), Stage II (energy micro-loss), Stage III (energy rapid loss), and Stage IV (elastic strain energy release). The distribution pattern of each energy density under different disturbance loadings remains generally consistent before reaching the stress peak. In Stage I, all the input energy is converted into elastic strain energy accumulated within the specimen. Flawed rock specimens under type-I and type-III disturbances then enter the energy micro-loss stage. During this stage, microcracks initiate and propagate at a slow rate, accompanied by plastic deformation. In contrast, no distinct Stage II is observed when flawed rock specimens are subjected to type-II disturbance loading. This could be due to the graded unloading of the confining pressure. The graded unloading of the confining pressure significantly affects the rate of crack initiation and coalescence, while the dissipated energy increases rapidly. In Stage III, the dissipated energy density u_d exceeds the elastic strain energy density u_e and continues to increase, while the elastic strain energy density tends to stabilize. Upon instability failure of the specimens, the energy evolution enters stage IV, where a significant decrease in elastic strain energy occurs under different disturbance loadings. It is worth noting that the peak elastic strain energy density, u_f, of the flawed rock specimens is at a low level under different disturbance loadings. The lowest peak elastic strain energy density of 0.4 MPa/m^3 is observed under type-II disturbance loading. The peak elastic strain energy densities are 0.8 MPa/m^3 and 0.79 MPa/m^3 for type-I and type-III disturbance loading, respectively. This indicates that confining pressure has a significant effect on the energy storage properties of the flawed rock specimens. The graded unloading of confining pressure leads to an abrupt weakening of the mechanical properties of the flawed rock specimens, their strength grading plummets, and the number of damaged units proliferates. This results in a decrease in the energy storage capacity of the flawed rock specimens and an accompanying abrupt increase in dissipated energy. When the confining pressure remains constant, the graded increasing cyclic disturbance loading results in a greater amplitude of cyclic deformation of the flawed rock specimens. This leads to an increase in the total energy input, which not only promotes the propagation of microcracks but also enhances energy dissipation, such as thermal and acoustic energy.

4.2. Characteristics of energy release

The accumulation of elastic strain energy in the early stage of

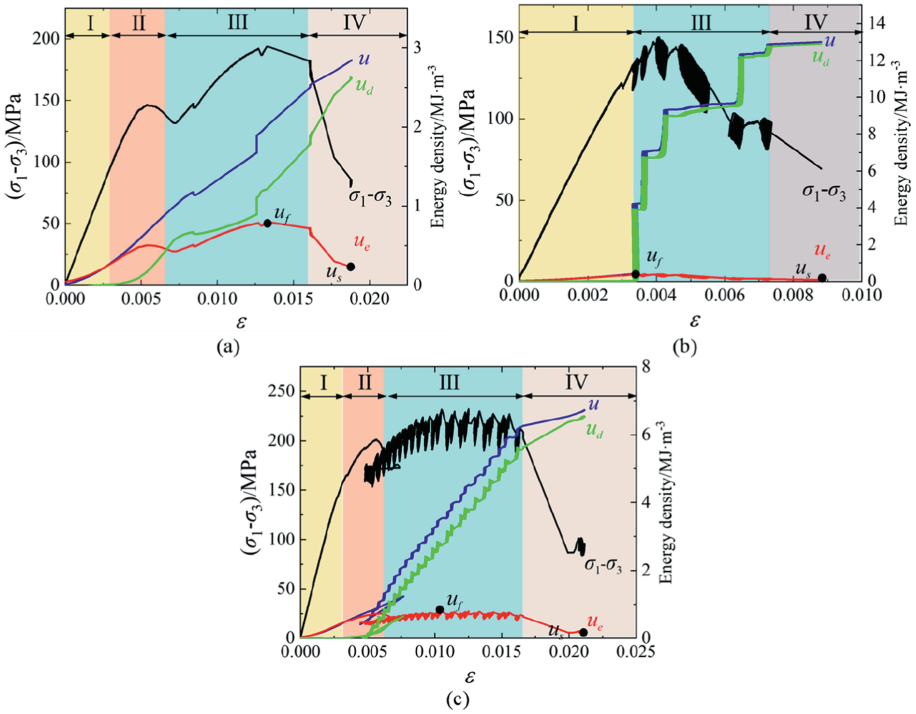

Fig. 9. Energy evolution process of test specimens under different disturbance loadings: (a) Type-I disturbance loading; (b) Type-II disturbance loading; and (c) Type-III disturbance loading.

loading depends on the energy storage properties of the rock material. After reaching the peak, its variation is controlled by damage accumulation and fracture evolution. As a characteristic parameter reflecting damage evolution, the faster the elastic strain energy is released during the disturbance phase, the more rapidly the rock undergoes failure.

The evolution of the elastic properties of the rock during the disturbance can be quantified by the parameter δ_e, which is defined as

$$\delta_e = \Delta u_e / \Delta t \tag{22}$$

where Δu_e is the change in elastic strain energy from the start of the disturbance to the end of the test at time Δt. The elastic strain energy ratio η_e is defined as

$$\eta_e = u_e / u \tag{23}$$

In addition, the release amount of elastic strain energy density u_a is defined as

$$u_a = u_f - u_s \tag{24}$$

where u_f is the peak strain energy density, and u_s is the residual strain energy density.

The variation in elastic strain energy density, the rate of evolution of the elastic strain energy density, and the proportion of elastic energy with time during the test are shown in Fig. 10. As observed in Fig. 10a, the elastic strain energy density peaks at 0.8 MJ/m^3, and the proportion of elastic energy, η_e, consistently decreases to 0.4 when the stress level peaks under type-I disturbance loading. This indicates that a large number of microcracks have formed in the specimen during the rapid energy loss stage, resulting in partial damage. Subsequently, the elastic strain energy decreases slightly when subjected to cyclic loading. The total input energy continues to increase, causing more micro-units to reach the critical stress state, initiate microcracks, and progressively increase the number of damaged units. From a macroscopic perspective, this is manifested by a reduction in the load-bearing capacity of the rock specimen and a decrease in its energy storage capacity. In the late stage of cyclic loading, the proportion of elastic energy in the specimen is about 0.25, and the elastic strain energy density is approximately 0.6 MJ/m^3. In addition, it is observed that the rate of evolution of the elastic strain energy density fluctuates around zero, but the phenomena of energy accumulation and dissipation remain significant. During this time, the mechanical energy supplied by the testing machine to the specimen is dissipated through various energy paths triggered by specimen deformation and crack propagation. The specimen undergoes structural instability failure when coplanar microcracks coalesce to form penetrating flaws. The elastic strain energy density in the specimen instantaneously drops to 0.21 MJ/m^3. The corresponding rate of elastic strain energy density evolution, δ_e, suddenly increases, reaching a maximum value of 10 MJ/(m^3 s). These results suggest that cyclic disturbances can cause a sudden release of elastic strain energy. From a microscopic perspective, plastic deformation occurs when a rock unit is subjected to a shear stress exceeding its strength according to the Mohr–Coulomb criterion. As a result, most of the elastic strain energy stored within the rock is rapidly converted into dissipative energy, which characterizes the failure of the rock. The flawed rock mass progressively accumulates microdamage under cyclic loading. The gradual reduction in elastic strain energy density characterizes the failure process, whereas the abrupt release of elastic strain energy signifies instability failure.

The evolutionary characteristics of the elastic strain energy under type-II disturbance loading are shown in Fig. 10b. The reduction in confining pressure leads to a decrease in the load-bearing capacity of the flawed rock specimens, resulting in a lower peak elastic strain energy density compared to type-I disturbance loading. Additionally, under type-II loading

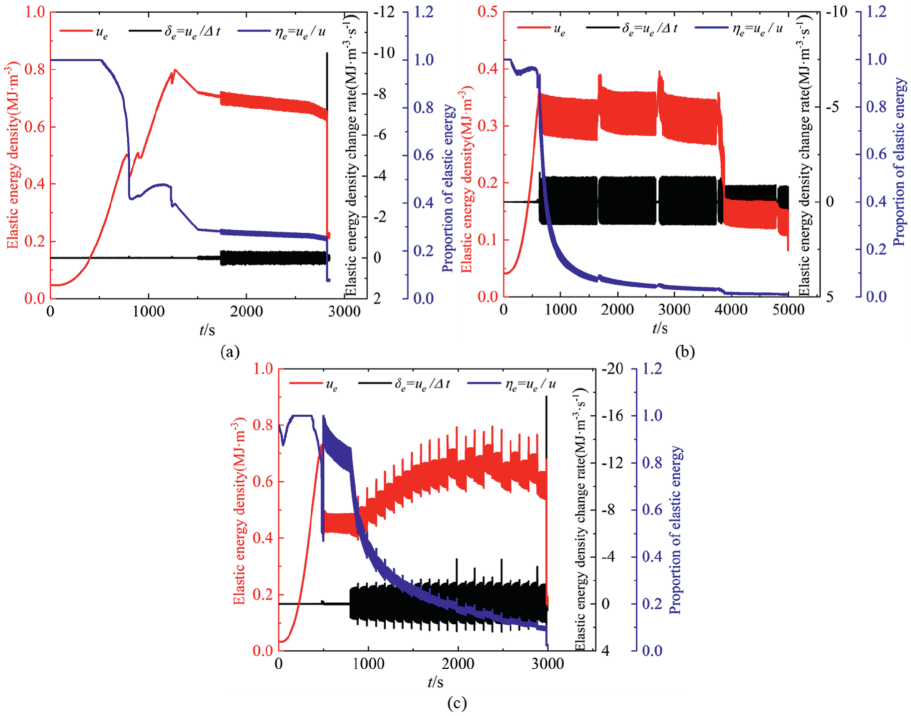

Fig. 10. Energy release characteristics of test specimens under different disturbance loadings: (a) Type-I disturbance loading; (b) Type-II disturbance loading; and (c) Type-III disturbance loading.

disturbance, the elastic strain energy density remains at its peak for a longer period. It is considered that the elastic rock units are relatively stable during this phase. The disturbance loads have not effectively increased the degree of damage to the specimen. Further reduction of the confining pressure promotes the damage caused by the disturbance loads to the rock specimen. From Fig. 10c, it can be observed that under type-III disturbance loading, the rate of evolution of elastic strain energy density is significantly higher than that under type-I disturbance loading due to the graded increase in the amplitude of the disturbance load. Meanwhile, Fig. 10c shows that the total energy input into the specimen under type-III disturbance loading increases during the disturbance phase. However, the proportion of elastic energy in the total energy decreases. As the amplitude of the disturbance load graded increases, the propagation path of coplanar cracks becomes more variable, potentially increasing the energy required for crack extension. When the specimen ultimately fails, the elastic strain energy in the specimen instantaneously drops to 0.16 MJ/m^3. The rate of evolution of the elastic strain energy density, δ_e, reaches 18.33 MJ/(m^3 s). This further indicates that the instantaneous energy release rate during the instability failure of the flawed rock specimen is higher under type-III disturbance loading.

Fig. 11 shows the characteristic values of elastic strain energy density under different types of disturbance loading. Clearly, the unloading effect of the confining pressure keeps the peak elastic strain energy density of the flawed rock specimens at a low level. Considering the influence of confining pressure on the mechanical constitutive behavior of rocks, a low confining pressure results in reductions in key parameters such as peak strength and peak strain. As a result, the energy storage capacity of the flawed rock specimens is significantly reduced, reaching only half of the value observed under other types of disturbance loading. A comparison of type-I and type-III loading effects shows that graded increasing cyclic loading does not alter the peak elastic strain energy density under the same confining pressure. This further demonstrates that confining pressure is the dominant factor influencing the energy storage capacity of flawed rock materials. However, the elastic strain energy release of the specimens under type-III disturbance loading is significantly increased. This indicates that graded increasing disturbance loading can effectively intensify damage in the flawed rock specimens.

5. Discussion

5.1. Crack initiation behavior under in situ stress

According to the strain energy density theory (Shih, 1981; Saribay, 2023), when the strain energy accumulates to the surface energy required to overcome crack propagation, microcracks can initiate and propagate as a pathway for energy dissipation. Considering the physical and mechanical properties of rock masses, such as heterogeneity and anisotropy, the spatial distribution characteristics of pre-existing flaws have varying degrees of influence on the mechanical behavior of rock masses (Liu et al., 2023). In deep geotechnical engineering, the inherent attribute of in situ stress leads to high confining pressure, which alters the mechanical properties and fracture characteristics of rock masses from the constitutive perspective. The nonlinear constitutive characteristics of the rock mass are further coupled with the spatial features of the non-persistent flaws, resulting in complex stress paths and variable failure characteristics in the flawed rock mass. The crack initiation angle at the tips of the flaw typically predicts the failure mode of the flawed rock mass. Therefore, understanding the crack initiation behavior of flawed rock masses under the coupled influence of mechanical boundary conditions and flaw spatial characteristics is crucial for the safe construction of deep geotechnical engineering.

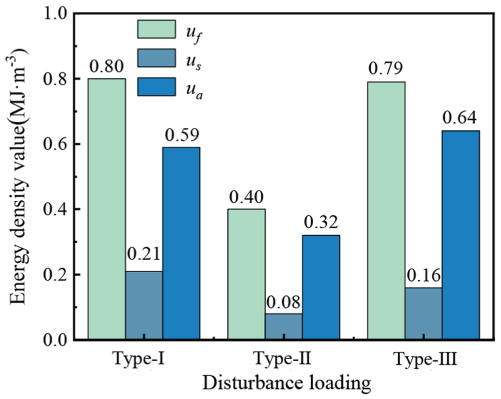

Fig. 11. Characteristic values of elastic energy density under different disturbance loadings.

Luo et al. (2022) investigated crack initiation stresses in granite specimens with prefabricated flaws under triaxial loading. They found that there is a strong functional relationship between crack initiation stresses, confining pressures, and the inclination angle of the flaws, as shown below:

$$\sigma_{ci} = \begin{cases} 132.545 - 99.094e^{-0.038\sigma_3} + \sigma_3 \quad (\beta = 30^\circ) \\ 0.693\left(\frac{\pi}{2} - \beta\right) + 108.424 \ (\sigma_3 = 40 \text{ MPa}) \end{cases} \tag{25}$$

When $\beta = 30^\circ$, the crack initiation angles can be obtained by substituting Eq. (25) into Eq. (16) under different confining pressures, and the distribution of values is shown in Fig. 12. A strong nonlinear functional relationship is observed between the crack initiation angle and confining pressure when the inclination of the flaws is consistent. The crack initiation angle increases gradually with increasing confining pressure. It is noted that the confining pressure provided by the testing machine is servo-controlled and remains constant during the loading process. In contrast, for extremely deep underground conditions, the rock mass around the surrounding rock mass can be idealized as a rigid boundary. During the loading process, the rigid boundary provides passive confining pressure on the flawed rock mass due to the deformation of the disturbed rock mass. This passive confining pressure progressively increases as the surrounding rock experiences accumulating damage during the disturbance process. This results in a more complex fracture behavior of the flawed rock mass. As shown

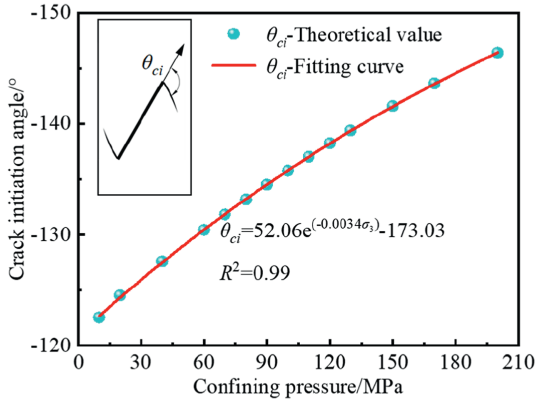

Fig. 12. The relationship between crack initiation angle and confining pressure.

in Fig. 13, at the beginning of loading, the additional passive confining pressure is small, and cracks initiate within a specific range. With the gradual increase in load, the deformation of the specimen increases, and the additional passive confining pressure increases significantly. Notably, the large deformation of the specimen indicates increased damage and higher crack density compared to those during the preloading period. The flawed rock mass eventually tends to fail through localized damage nucleation around the pre-existing flaws.

Based on the findings of Luo et al. (2022), the distribution of crack initiation angles with varying flaw inclinations under a constant confining pressure of 40 MPa (σ_3) is shown in Fig. 14. A linear relationship exists between the crack initiation angle and the inclination angle of the flaw (β). The crack initiation angle gradually decreases as β increases, which is consistent with experimental observations. Combined with Figs. 12 and 14, it is evident that both the confining pressure and the inclination angle of the flaw significantly influence the crack initiation angle. Considering the heterogeneous properties of the rocks, the changes in the crack initiation angle caused by the increase in confining pressure are relatively minor. However, under rigid boundary conditions, the passive confining pressure results in a more complex microcrack distribution within the flawed rock mass, accompanied by variable failure paths. The influence of the flaw inclination angle β on the crack initiation angle exerts a more intuitive influence.

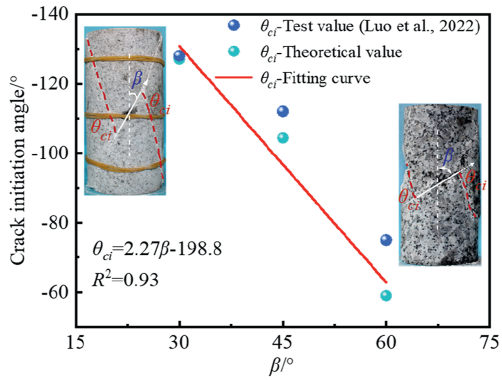

Fig. 14. The relationship between crack initiation angle and the inclination angle of the flaw (β).

5.2. Fracture modes under different disturbance loadings

The construction conditions in underground engineering are complex, and engineering rock masses experience variable loading conditions. Based on the elastoplastic constitutive behavior and diagenetic mechanisms of rock, the deformation of the rock mass under loading can be divided into four stages: compaction, elastic deformation, plastic deformation, and instability. The crack initiation phenomenon characterizes a rock mass entering the plastic deformation stage. Flawed rock masses experience disturbance from engineering loads, typically comprising a combination of dynamic and static loads. When the axial static load remains below the crack initiation stress of the flawed rock mass, the fracture behavior is predominantly governed by the additional cyclic disturbance loading. Therefore, analyzing the dynamic fracture behavior of the flawed rock mass induced by additional cyclic loading is crucial. Such analysis, incorporating different types of disturbance loading, is vital for revealing rock mass failure mechanisms. It facilitates a comprehensive understanding of failure behavior under complex stress fields.

Under type-I disturbance loading, the flawed rock specimens remain in the elastic deformation stage, as indicated by the stress–strain relationship. They undergo reciprocal elastic deformation under cyclic loading. Numerous studies have shown that the crack initiation stress of rocks is about 40 % of the peak stress (Palchik, 2014; Li et al., 2024b), and the fatigue strength of rock masses is about 80 % of the peak strength (Geranmayeh Vaneghi et al., 2020). Consequently, when the cyclic stress amplitude remains below the crack initiation stress, the flawed rock specimens do not enter the plastic deformation stage. The reduction in confining pressure under type-II disturbance loading results in the reduction of mechanical properties, such as strength and elastic modulus of the flawed rock specimens. As a result, flawed rock specimens undergo fracture when the disturbance load amplitude reaches at least 40 % of their compressive strength. The mode of initial crack initiation depends on whether confining pressure is present when the fracture occurs. Under confining pressure, the initial fracture is dominated by anti-wing cracks, leading to shear failure. In the absence of confining pressure, the initial fracture is dominated by wing cracks, resulting in tensile failure. When the disturbance load amplitude exceeds the threshold value for fatigue

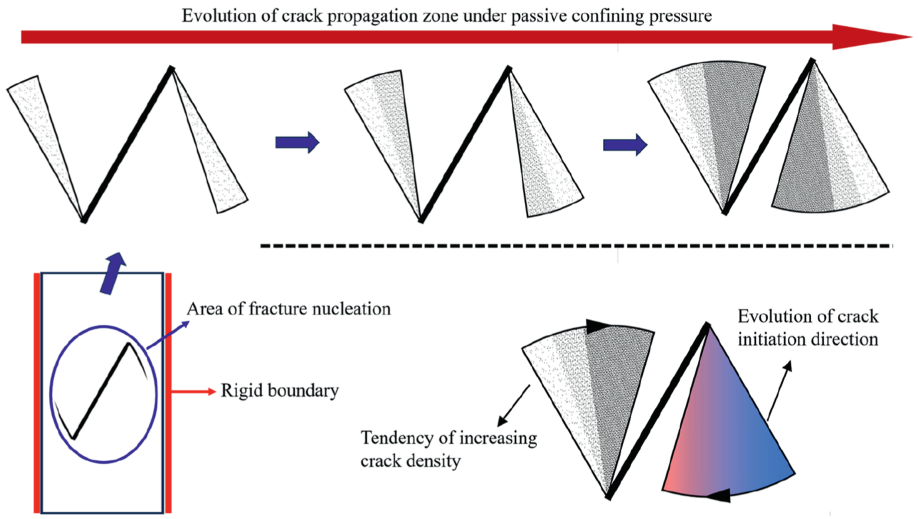

Fig. 13. Fracture behavior of flawed rock masses under passive confining pressure.

failure of the flawed rock specimens, macroscopic penetrating cracks with variable propagation directions form due to accumulated fatigue damage. Under type-III disturbance loading, the cyclic load amplitude is gradually increased. When it reaches the crack initiation stress, the tips of the non-persistent flaw rapidly accumulate strain energy due to stress concentration, leading to the initiation of anti-wing cracks. However, localized stress redistribution and continuous loading-unloading cycles result in variable crack propagation directions. Notably, when considering the in situ stress environment, brittle rock masses with non-persistent flaws typically exhibit similar failure patterns under external loading. You et al. (2022) conducted coupled dynamic-static loading experiments on rock-like specimens with a single flaw using a split Hopkinson pressure bar (SHPB) system. The failure patterns observed under impact loading disturbance were consistent with those identified in the present study. That is, the specimens ultimately experienced shear failure resulting from the coalescence and penetration of anti-wing cracks and coplanar cracks. Similarly, Lu et al. (2021) observed this phenomenon in their study on fracture evolution in mudstone with a single flaw.

In summary, when the static load does not reach the crack initiation stress of the flawed rock mass, cyclic loading will not trigger crack initiation, and it remains in a stable state. The fracture behavior of the flawed rock mass is jointly governed by its mechanical properties and the loading path under type-II disturbance loading. Under graded increasing cyclic loading, anti-wing cracks in flawed rock masses initiate from the flaw tips and experience shear failure.

5.3. Engineering applications of rock fracture mechanisms

Owing to safety and economic considerations, deep geotechnical engineering often adopts the design scheme of pilot tunnel excavation. The complex configuration of construction-induced load disturbances leads to spatiotemporal damage effects, substantially increasing the risk of further deterioration in engineering rock masses. Therefore, promptly addressing both visible and potential risks is essential to ensuring construction progress and engineering quality.

This study elucidates the fracture mechanisms governing flawed rock masses under construction disturbance loading, as illustrated in Fig. 15a, and further analyzes the propagation paths of non-persistent flaws. These findings provide a theoretical foundation for disaster prevention and mitigation in deep underground engineering. Fig. 15b illustrates the distribution of fracture surfaces of flaw A under type-III disturbance loading during sequential excavation operations at different working faces. Reinforcement measures are necessary for fracture surfaces that may lead to slip fractures in the surrounding rock. Based on the fracture paths and potential slip surface characteristics clarified in this study, bolt reinforcement design schemes can be further optimized by accounting for the on-site construction conditions. As shown in Fig. 15b, the installation of rock bolts perpendicular to structural planes optimizes the provision of normal stress, thereby enhancing the shear resistance of fracture surfaces. The targeted arrangement of bolts promotes coordinated stress redistribution in surrounding rock masses. This configuration effectively reduces the likelihood of shear-slip failure while enhancing the overall stability of the rock mass. Furthermore, the research findings enable the prediction of fracture angles in non-persistent flaws and potential crack propagation paths, providing a theoretical basis for grouting reinforcement design. Evaluating the initiation and propagation directions of non-persistent flaws based on in situ stress conditions provides reliable guidance for optimizing grout diffusion orientation. This methodology not only enhances grouting efficacy but also effectively blocks fracture propagation paths in the rock mass promptly.

The fracture behavior of flaw B under type-II disturbance loading is shown in Fig. 15c. In the presence of abundant groundwater, unfavorable geological formations are prone to developing macroscopic fracture planes under construction-induced disturbances, which may lead to water and mud inrush. The fracture behaviors observed in flawed rock masses in this study provide precise and reliable spatial and directional guidance for damage zone detection. This approach enhances both detection efficiency and accuracy. Based on the detection results, timely advanced grouting measures can be implemented to consolidate fractured rock blocks, forming a grout curtain, thereby effectively blocking groundwater flow paths. Additionally, the formation of penetrating fracture surfaces between the excavated zone and the surrounding rock mass may trigger rockfalls within the chamber. To ensure construction safety, advanced support measures should be implemented at potential fracture surfaces.

In summary, the findings regarding the mechanical response characteristics of flawed rock masses can be directly applied to designing excavation and reinforcement schemes for underground chambers. This advancement significantly enhances the timeliness and reliability of disaster prevention and mitigation in deep underground engineering.

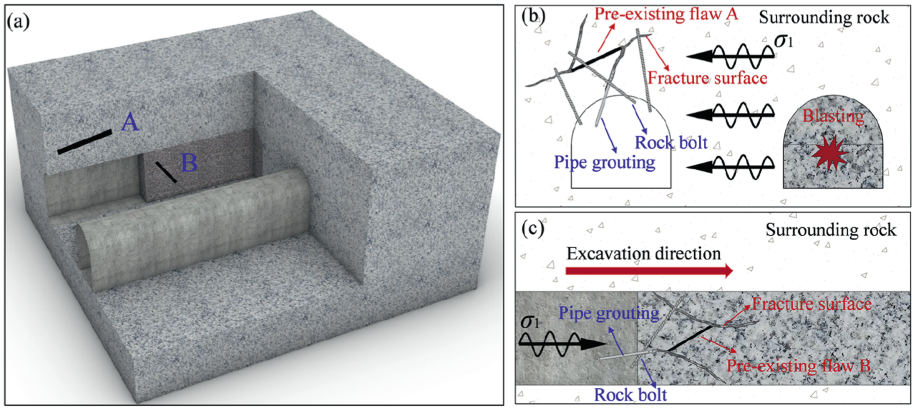

Fig. 15. Fracture behavior of rock masses with a non-persistent flaw for engineering applications: (a) Schematic locations of non-persistent flaws; (b) The reinforcement treatment for flaw A; and (c) The reinforcement treatment for flaw B.

6. Conclusions

The present study employed cyclic disturbance loading with a frequency of 5 Hz and an amplitude of 0.03 mm. Three cyclic loading and unloading paths were designed to investigate the mechanical properties and failure mechanisms of granite with non-persistent flaws under a confining pressure of 40 MPa. The crack initiation angle was calculated using the MTS criterion. A fracture mechanics model for open flaws was developed to investigate the intrinsic response of crack initiation behavior to confining pressure and flaw spatial characteristics. The main conclusions are as follows:

(1) Graded unloading of confining pressure under identical cyclic loading significantly degrades the mechanical properties of flawed rock specimens, reducing the peak stress to only 77.5 % of that under constant confining pressure. In contrast, graded increasing cyclic loading significantly enhances the load-bearing capacity of flawed rock specimens, resulting in a peak stress 19.3 % higher than that under constant cyclic disturbance loading.
(2) The flawed rock specimens exhibit predictable fracture propagation paths under triaxial disturbance loading conditions. Shear-induced anti-wing cracks represent the fundamental fracture pattern. Coplanar and wing cracks do not initiate independently, but rather develop in conjunction with other crack types, serving as supplementary mechanisms for stress release. Notably, wing crack initiation occurs exclusively under confining pressure unloading conditions.
(3) Under a constant confining pressure of 40 MPa, the type of disturbance loading exerts no significant effect on the failure mode. The flawed granite specimens develop a nearly V-shaped failure zone along the open flaw, characterized by shear failure. However, unloading of the confining pressure induces a complex shear-tensile failure mode in the flawed granite specimens.
(4) Confining pressure exerts a significant influence on the energy storage characteristics of the flawed granite specimens. Under graded unloading of confining pressure, the peak elastic strain energy density is reduced to approximately 50 % of the value observed under constant confining pressure. Moreover, graded increasing disturbance loading effectively intensifies the damage sustained by the flawed rock specimens.
(5) The crack initiation angle exhibits a nonlinear increase with confining pressure, but gradually decreases with increasing flaw inclination angle (β). Under passive confining pressure, secondary crack coalescence and propagation zones progressively shrink inward, leading to localized nucleation failure around the pre-existing flaw in granite.

It should be noted that the conclusions drawn from this study are subjected to certain limitations. Diagenetic processes impart distinct microstructural characteristics to different rock types, which, in turn, significantly influence their fracture behavior and failure mechanisms. Furthermore, variations in confining pressure and disturbance loading frequency may further modify these fracture responses. Therefore, future work should conduct systematic studies across a broader range of rock materials to develop universally applicable fracture criteria.

CRediT authorship contribution statement

Tingting Liu: Writing – original draft, Methodology, Funding acquisition, Conceptualization. **Chao Zhang:** Writing – original draft, Methodology, Data curation. **Luyang Ding:** Writing – review & editing, Visualization, Investigation. **Kun Xu:** Investigation, Data curation. **Xinping Li:** Methodology, Conceptualization. **Wenxu Huang:** Resources, Data curation.

Declaration of competing interest

The authors declare that they have no known competing financial interests or personal relationships that could have appeared to influence the work reported in this paper.

Acknowledgments

The research was financially supported by the National Natural Science Foundation of China (Grant Nos. 52079102 and 52279108), and the Hubei Provincial Natural Science Foundation (Grant No. 2024AFA041).

Nomenclature

σ_1	Axial pressure
σ_3	Confining pressure
P	Density
V_p	P-wave velocity
E_s	Young modulus
μ	Poission's ratio
u_{ics}	85 % of the mean peak stress
f	Disturbance frequency
D_v	Amplitude of disturbance load
ε_v	Volumetric strain
ε_1	Axial strain
ε_3	Radial strain
ε_{vp}	Peak value of volumetric strain
ε_{vz}	Zero point of volumetric strain
ε_{vf}	Final value of volumetric strain
V_0	The volume of the material before deformation
V	The volume of the material after deformation
ε_s	Eigenvalue of axial strain
σ_N	Normal stress distributed on the flaw surface
K_I	Stress intensity factors in mode I
K_{II}	Stress intensity factors in mode II
Y	Boundary correction factor
T_x	Parallel non-singular stress
T_y	Perpendicular non-singular stress
σ_r	Radial stress field at the tip of the flaw
σ_θ	Tangential stress field at the tip of the flaw
$\tau_{r\theta}$	Shear stress field at the tip of the flaw
σ_c	Crack initiation stress
θ_c	Crack initiation angle
U	Total energy
U_e	Elastic strain energy
U_d	Dissipated energy
u	Energy density
u_1	Axial total strain energy density
u_3	Radial total strain energy density
E_t	Elastic modulus of the rock at time t
ν_t	Poisson's ratio of the rock at time t

u_f	Peak elastic strain energy density
u_s	Residual strain energy density
δ_e	Rate of change of elastic strain energy density
η_e	Elastic strain energy ratio
Δu_e	Change in elastic strain energy density from the start of the disturbance to the end of the test at time Δt
u_a	Release amount of elastic strain energy density

References

Chai, Y.J., Dou, L.M., Cai, W., et al., 2023. Experimental investigation into damage and failure process of coal-rock composite structures with different roof lithologies under mining-induced stress loading. Int. J. Rock Mech. Min. Sci. 170, 105479.

Chang, X., Zhang, X., Dang, F.N., Zhang, B.F., Chang, F.Q., 2022. Failure behavior of sandstone specimens containing a single flaw under true triaxial compression. Rock Mech. Rock Eng. 55 (4), 2111–2127.

Chen, L.G., Wang, D., Jiang, Y., Liu, J.K., Luan, H.J., Wu, C.Y., 2024. Study on the failure modes of water-bearing soft rock under different low-frequency disturbance. Eng. Fail. Anal. 164, 108683.

Chen, Q.G., Zuo, Y.J., Zheng, L.J., 2025. Deformation failure mechanism and stability-control technology of deep layered clastic-rock roadway under dynamic disturbance. Tunn. Undergr. Space Technol. 156, 106255.

Cui, Z., Dai, F., Liu, Y., Zhang, B., Wei, M., Zhang, Q., 2024. Dynamic fracture properties and criterion of cyclic freeze-thaw treated granite subjected to mixed-mode loading. J. Rock Mech. Geotech. Eng. 16, 4971–4989.

Geranmayeh Vaneghi, R., Thoeni, K., Dyskin, A.V., Sharifzadeh, M., Sarmadivaleh, M., 2020. Fatigue damage response of typical crystalline and granular rocks to uniaxial cyclic compression. Int. J. Fatig. 138, 105667.

Gong, H., Luo, Y., Xu, K., Huang, J., Wang, G., Li, X., 2022. Failure behaviors of fractured granite during loading and unloading under high confining pressure based on acoustic emission multi-parameter analysis. Theor. Appl. Fract. Mech. 121, 103442.

Goss, R.N., 1964. Some basic problems of the mathematical theory of elasticity (N. I. Muskhelishvili). SIAM Rev. 6 (3), 320–321.

Guo, J.Q., Liu, P.F., Fan, J.Q., Shi, X.Y., Huang, X., 2021. Influence of confining pressure unloading rate on the strength characteristics and fracture process of granite using lab tests. Adv. Mater. Sci. Eng. 2021, 7925608.

Haeri, H., Sarfarazi, V., Zhou, L., Karimi Javid, H., Asgari, K., Elahi, A., 2024. Evaluation of rock pillar failure mechanisms under uniaxial compression: impact of joint number and joint angle. Comput. Part. Mech. 12, 205–230.

Hou, K., Zhu, M., Hao, Y., Yin, Y., An, L., 2023. Stability analysis and evaluation of surrounding rock of ultra-deep shaft under complicated geological conditions. Front. Earth Sci. 11, 1216667.

Hu, L.H., Li, Y.C., Liang, X., Tang, C.A., Yan, L.B., 2020. Rock damage and energy balance of strainbursts induced by low frequency seismic disturbance at high static stress. Rock Mech. Rock Eng. 53 (11), 4857–4872.

Hu, L.H., Ma, K., Liang, X., Tang, C.N., Wang, Z.W., Yan, L.B., 2018. Experimental and numerical study on rockburst triggered by tangential weak cyclic dynamic disturbance under true triaxial conditions. Tunn. Undergr. Space Technol. 81, 602–618.

Irwin, G.R., 1957. Analysis of stresses and strains near the end of a crack traversing a plate. J. Appl. Mech. 24 (3), 361–364.

Jiang, Y.J., Liang, B., Wang, D., Luan, H.J., Zhang, G.C., Dong, L., Chen, L.G., 2024. Experimental study on failure mechanical properties and acoustic emission characteristics of soft rock–coal combination under dynamic disturbance. Eng. Fail. Anal. 158, 108016.

Li, H., Zhong, R.Z., Pel, L., Smeulders, D., You, Z.J., 2024b. A new volumetric strain-based method for determining the crack initiation threshold of rocks under compression. Rock Mech. Rock Eng. 57 (2), 1329–1351.

Li, J.C., Nie, M.M., Li, X., 2023. Study of stress wave propagation across a non-persistent joint based on a boundary integral equation method. Geomech. Geophys. Geo-Energy Geo-Resour. 9 (1), 56.

Li, L.Y., Xie, H.P., Ma, X., Ju, Y., Tang, T.W., Fang, Q.J., 2012. Experimental study on relationship between surface temperature and volumetric strain of rock under uniaxial compression. J. Chian. Coal Soc. 37 (9), 1511–1515 (in Chinese).

Li, X.B., Zhou, Z.L., Lok, T., Hong, L., Yin, T.B., 2008. Innovative testing technique of rock subjected to coupled static and dynamic loads. Int. J. Rock Mech. Min. Sci. 45 (5), 739–748.

Li, Y.D., Han, L., Shang, T., 2024a. Energy evolution and brittleness analysis of sandstone under confining pressure unloading. Rock Mech. Rock Eng. 57 (7), 4729–4754.

Liang, B., Wang, D., Jiang, Y.J., Luan, H.J., Liu, J.K., Wang, J.L., 2024. Analysis of fracture modes and acoustic emission characteristics of low-frequency disturbed coal rock bodies with different cyclic amplitudes. Fatig. Fract. Eng. Mater. Struct. 47 (12), 4412–4431.

Lin, J., Zuo, Y., Wang, J., Zheng, L., Chen, B., Sun, W., Liu, H., 2020. Stability analysis of underground surrounding rock mass based on block theory. J. Cent. South Univ. 27 (10), 3040–3052.

Liu, K., Zhang, Q.B., Wu, G., Li, J.C., Zhao, J., 2019. Dynamic mechanical and fracture behaviour of sandstone under multiaxial loads using a triaxial hopkinson bar. Rock Mech. Rock Eng. 52 (7), 2175–2195.

Liu, M., Liu, E., 2017. Dynamic mechanical properties of artificial jointed rock samples subjected to cyclic triaxial loading. Int. J. Rock Mech. Min. Sci. 98, 54–66.

Liu, T., Ding, L., Wang, G., Ma, R., Li, X., 2023. Dynamic properties and failure mechanism of granite with non-persistent joints subjected to impact load. Int. J. Rock Mech. Min. Sci. 169, 105451.

Liu, T.T., Zhang, C., Li, X.P., Xu, K., Xu, M.N., Wang, Z.X., 2024b. Triaxial experimental study of mechanical behavior of non-persistent jointed granite subjected to slight cyclic dynamic disturbances. Theor. Appl. Fract. Mech. 130, 104254.

Liu, X.S., Ning, J.G., Tan, Y.L., Gu, Q.H., 2016. Damage constitutive model based on energy dissipation for intact rock subjected to cyclic loading. Int. J. Rock Mech. Min. Sci. 85, 27–32.

Liu, Y., He, B., Dai, F., Zhang, Q., Liu, Y., 2024a. Mechanical responses of chemically corroded sandstone under cyclic disturbance: insights from fatigue properties and macro-micro fracturing mechanism. Int. J. Rock Mech. Min. Sci. 180, 105818.

Lu, Y., Pu, H., Wang, L., Li, Z., Meng, X., Wang, B., Zhang, K., 2021. Fracture evolution in mudstone specimens containing a pre-existing flaw under true triaxial compression. Int. J. Rock Mech. Min. 138, 104594.

Luo, Y., Gong, H.L., Xu, K., Pei, C.H., Wei, X.Q., Li, X.P., 2022. Progressive failure characteristics and energy accumulation of granite with a pre-fabricated fracture during conventional triaxial loading. Theor. Appl. Fract. Mech. 118, 103219.

Ma, C.D., Long, S., Li, X.B., Liu, Z.L., Xie, W.B., 2020. Research and microscopic analysis of seepage characteristics of sandstone under low-frequency cyclic loading. IOP Conf. Ser. Earth Environ. Sci. 570 (5), 52048.

Ma, J., Dong, L., Zhao, G., Li, X., 2019. Focal mechanism of mining-induced seismicity in fault zones: a case study of yongshaba mine in China. Rock Mech. Rock Eng. 52 (9), 3341–3352.

Melin, S., 1986. Fracture from a straight crack subjected to mixed mode loading. Int. J. Fract. 32 (4), 257–263.

Meng, F.Z., Yue, Z.F., Zhou, X., et al., 2024. Fracture slip behavior in granite under high-temperature true triaxial loading tests. Rock Mech. Rock Eng. 57 (11), 9669–9694.

Modiriasari, A., Bobet, A., Pyrak-Nolte, L.J., 2017. Active seismic monitoring of crack initiation, propagation, and coalescence in rock. Rock Mech. Rock Eng. 50 (9), 2311–2325.

Palchik, V., 2014. Use of descartes folium equation for deriving a relation between total aperture of fractures after uniaxial compression and strain parameters of different rocks exhibiting negative total volumetric strains. Rock Mech. Rock Eng. 47 (6), 2075–2086.

Peng, R.D., Ju, Y., Wang, J.G., Xie, H.P., Gao, F., Mao, L.T., 2015. Energy dissipation and release during coal failure under conventional triaxial compression. Rock Mech. Rock Eng. 48 (2), 509–526.

Ran, Q.C., Chen, P., Liang, Y.P., et al., 2024. Hardening-damage evolutionary mechanism of sandstone under multi-level cyclic loading. Eng. Fract. Mech. 307, 110291.

Saribay, M., 2023. Effect of stress wave propagation phenomenon on the determination of strain energy density theory parameters and dynamicj -integral. Fatig. Fract. Eng. Mater. Struct. 46 (1), 63–79.

Shan, R., Bai, Y., Ju, Y., Han, T., Dou, H., Li, Z., 2021. Study on the triaxial unloading creep mechanical properties and damage constitutive model of red sandstone containing a single ice-filled flaw. Rock Mech. Rock Eng. 54 (2), 833–855.

Shi, Z.M., Li, J.T., Wang, J., 2022b. Effect of creep load on fatigue behavior and acoustic emission characteristics of sandstone containing pre-existing crack during fatigue loading. Theor. Appl. Fract. Mech. 119, 103296.

Shi, Z.M., Li, J.T., Wang, J., 2022a. Research on the fracture mode and damage evolution model of sandstone containing pre-existing crack under different stress paths. Eng. Fract. Mech. 264, 108299.

Shih, C.F., 1981. Relationships between the j-integral and the crack opening displacement for stationary and extending cracks. J. Mech. Phys. Solid. 29 (4), 305–326.

Su, G.S., Hu, L.H., Feng, X.T., et al., 2018. True triaxial experimental study of rockbursts induced by ramp and cyclic dynamic disturbances. Rock Mech. Rock Eng. 51 (4), 1027–1045.

Tang, S.B., 2015. The effect of t-stress on the fracture of brittle rock under compression. Int. J. Rock Mech. Min. Sci. 79, 86–98.

Tang, X., Wan, W., Chen, W., Zhang, Z., 2023. Analysis of fracture characteristics of ore rock based on gmts criterion. KSCE J. Civ. Eng. 27 (10), 4352–4361.

Wang, H.Y., Pasternak, E., Dyskin, A., Dight, P., Zhou, Y., 2024b. Rock fractures developed in the class II post-peak unloading. Eng. Fract. Mech. 302, 110060.

Wang, J., Li, J.T., Shi, Z.M., Chen, J.C., 2022. Fatigue damage and fracture evolution characteristics of sandstone under multistage intermittent cyclic loading. Theor. Appl. Fract. Mech. 119, 103375.

Wang, Y., Chen, L.L., Wu, Y.F., Yi, X.F., 2024c. Cyclic fatigue responses of double fissure-contained marble: insights from mechanical responses, energy conversion and hysteresis characteristics. Theor. Appl. Fract. Mech. 134, 104750.

Wang, Y., Chen, Z.Z., Yi, X.F., Long, D.Y., 2024a. Macro-meso damage cracking and energy dissipation of rock-backfill composites: effect of cyclic disturbance frequency. Fatig. Fract. Eng. Mater. Struct. 47 (8), 2969–2987.

Wang, Y., Liu, D., Han, J., Li, C., Liu, H., 2020. Effect of fatigue loading-confining stress unloading rate on marble mechanical behaviors: an insight into fracture evolution analyses. J. Rock Mech. Geotech. Eng. 12, 1249–1262.

Wang, Y., Tang, P.F., Han, J.Q., Li, P., 2023a. Influence of dynamic disturbed frequency on rock failure characteristics under triaxial cyclic and multistage

unloading confining pressure loads. Fatig. Fract. Eng. Mater. Struct. 46 (4), 1527–1544.
Wang, Y., Tang, P.F., Li, P., Xia, Y.J., 2023b. Effect of disturbed frequency on rock failure and energy characteristics exposed to triaxial fatigue and multistage unloading confining pressure (TF-MSUCP) conditions. Eng. Fail. Anal. 145, 106997.
West, I., Walton, G., Diederichs, M., 2024. Evaluating the effects of joint set properties on laboratory rockmass analog specimen strength using bonded block models. Rock Mech. Rock Eng. 58, 4543–4568.
Xiao, F., Jiang, D.Y., Wu, F., Zou, Q.L., Chen, J., Chen, B., Sun, Z.G., 2020. Effects of prior cyclic loading damage on failure characteristics of sandstone under true-triaxial unloading conditions. Int. J. Rock Mech. Min. Sci. 132, 104379.
Xie, H.P., Ju, Y., Li, L.Y., 2005. Criteria for strength and structural failure of rocks based on energy dissipation and energy release principles. Chin. J. Rock Mech. Eng. 24 (17), 3003–3010 (in Chinese).
Xing, W., Xing, H., Cai, W., Li, X., Qiu, Y., Wang, M., 2024. Experimental study on dilatancy behavior of soft rock under dynamic loading. Int. J. Rock Mech. Min. Sci. 182, 105867.
Xing, Y., Kulatilake, P.H.S.W., Sandbak, L.A., 2018. Investigation of rock mass stability around the tunnels in an underground mine in USA using three-dimensional numerical modeling. Rock Mech. Rock Eng. 51, 579–597.
Xu, X., Jing, H.W., Liu, H.X., Zhang, L., Cai, J.M., Yin, Q., Li, H., 2023. Experimental investigation on strength-weakening effect and fracture behavior of red sandstone under coupled static and dynamic cyclic loadings. Theor. Appl. Fract. Mech. 123, 103723.
Yang, C., Tang, J.T., Huang, D., Wang, L.H., Sun, Q.C., Hu, Z.X., 2021. New crack initiation model for open-flawed rock masses under compression–shear stress. Theor. Appl. Fract. Mech. 116, 103114.
Yang, F.J., Hu, D.W., Zhou, H., Lu, J.J., 2020. Physico-mechanical behaviors of granite under coupled static and dynamic cyclic loadings. Rock Mech. Rock Eng. 53 (5), 2157–2173.
Yang, S., Yin, P., Zhang, Y., Chen, M., Zhou, X., Jing, H., Zhang, Q., 2019. Failure behavior and crack evolution mechanism of a non-persistent jointed rock mass containing a circular hole. Int. J. Rock Mech. Min. Sci. 114, 101–121.
Yao, W., Yu, J., Liu, X.Y., Zhang, Z.Q., Feng, X.W., Cai, Y.Y., 2023. Experimental and theoretical investigation of coupled damage of rock under combined disturbance. Int. J. Rock Mech. Min. Sci. 164, 105355.
You, W., Dai, F., Liu, Y., 2022. Experimental and numerical investigation on the mechanical responses and cracking mechanism of 3D confined single-flawed rocks under dynamic loading. J. Rock Mech. Geotech. Eng. 14 (2), 477–493.
Zhang, Q.B., Zhao, J., 2014. A review of dynamic experimental techniques and mechanical behaviour of rock materials. Rock Mech. Rock Eng. 47 (4), 1411–1478.
Zhang, S., Xu, D., Qiu, S., Feng, G., Jiang, Q., 2024. A fatigue damage model for sandstone based on acoustic emission and resistivity parameters. Constr. Build. Mater. 438, 137286.
Zhong, C.L., Zhang, Z.Y., Ranjith, P.G., Zhang, C.P., Xue, K.S., 2022. The role of pore pressure on the mechanical behavior of coal under undrained cyclic triaxial loading. Rock Mech. Rock Eng. 55 (3), 1375–1392.
Zhou, Y., Liu, H., 2023. The initiation criterion for open-crack considering fissured water under biaxial compression. Theor. Appl. Fract. Mech. 126, 103943.

Tingting Liu is a Professor at the School of Civil Engineering and Architecture, Wuhan University of Technology, China. She received her BSc degree from Zhengzhou University and PhD degree from the Institute of Rock and Soil Mechanics, Chinese Academy of Sciences. Her research interests encompass dynamic mechanical behavior of deep jointed rock masses, stress wave propagation across rock joints, prediction of blasting vibration, and safety assessment methodologies for deep underground surrounding rock.